Estimation of the effective elastic constants of bone scaffolds fabricated by direct ink writing

Petr Skalka[1], Karel Slámečka[1*], Edgar B. Montufar[1], Ladislav Čelko[1]

[1]CEITEC – Central European Institute of Technology, Brno University of Technology, Purkyňova 123, 612 00 Brno, Czech Republic

*Corresponding author:

E-mail address: karel.slamecka@ceitec.vutbr.cz,

Tel.: (+420) 54114 2812

Fax: +420 541 142 842

Keywords

Bone scaffold, Direct ink writing, Bioceramics, Effective elastic constants, Finite element modelling

Abstract

Direct ink writing is a popular method for fabrication of scaffolds, yet its widespread usage in clinical practice requires guarantee of compatibility of a scaffold with bone tissues. Mechanical compatibility is mandatory to prevent stress shielding and is expressed using the difference between effective elastic constants (EECs) of a scaffold and a tissue. In this paper, the solution for EECs of a calcium phosphate scaffold is derived for any combination of input parameters, inclusive of the contact radius at the joints, a feature arising mainly from the rheological properties of the ink. The model was validated by comparison with data from the literature and those obtained from tests on produced scaffolds and monoliths. The contact radius significantly influences elastic response, especially for small overlap between the printed layers. The inverse solution can be used for estimation of bulk properties but is also helpful for quality assessment of the fabrication process.

1. Introduction

Tissue engineering allows to enhance bone regeneration processes based on the structural and biological support for a newly formed tissue. Scaffolds made from calcium phosphate ceramics, bioactive glasses, polymers, or composites of these are often used for this purpose since they exhibit good biocompatibility, osteointegration, osteoconductivity, and bioresorbability [1-4]. Nowadays, the scaffolds are produced by several methods among which the direct ink writing (DIW, or robocasting) holds many promises [5, 6]. DIW is an extrusion solid freeform fabrication method that uses an ink to produce three-dimensional (3D) grid structures with well controlled porosity. In fact, the porosity (both intrinsic and external) is an important factor for bone tissue formation and the bone regeneration process proliferates from optimized pore size [3, 4, 7, 8]. At the same time, high porosity adversely affects mechanical properties of a scaffold and there is a trade-off between the mechanical and biological functions, which is particularly relevant to weak or fast-dissolving materials.

The geometry of a scaffold fabricated by DIW is mainly determined by computer aided design (CAD). Most deposition robots follow the NIST RS274NGC G-code standard to control the movements of the extrusion head. Among the different options to generate G-codes, the use of an automatic slicing program, such as Slic3r or Cura, is one of the most attractive alternatives, especially for users without programming experience. In general, the software slices a CAD model into layers and generate the code needed to print the object layer by layer. Despite losing some freedom, slicing programs allow the user to set up important geometrical parameters such as the deposition pathway, the diameter of the deposited rod, (which physically depends on the diameter of the nozzle used for extrusion), the distance between the rods (defined by an infill density), and the overlap between

consecutive layers, which assures formation of rigid joints linking the rods. After deposition, ceramic or glass objects are commonly dried and sintered to increase their mechanical strength. As can be expected, printing, drying and sintering conditions affect the final geometry of the object as well and geometrical distortions and cracks may be generated at these stages. Nonetheless, the quality assessment of printed scaffolds is usually limited to dimensional accuracy and observations on large cracks (if present) while the fine details are only rarely studied.

An interesting feature common in DIW scaffolds is the contact radius (an idealization of rounded connections at the joints), the geometry of which arises mainly from the rheological properties of the ink rather than the parameters set in the G-code. This geometrical attribute is important in particular for brittle materials since it determines stress concentration and load transfer in the structure. The available experimental evidence suggests that the contact radius ranges from only a few to more than several tens of percent of the diameter of the rod. For instance, the contact radius observed in magnesium-doped wollastonite/β-tricalcium phosphate scaffolds fabricated recently by Shao et. al [9] is ~3.5 %, similarly to that of 45S5 bioactive glass scaffolds prepared by Eqtesadi et. al [10]. On the other hand, the contact radius of 6P53B glass scaffolds described by Fu et. al [6] appears to be ~35 % on average, which was one of the reasons for unprecedentedly high compressive strength (136 MPa at 60% porosity) of these scaffolds, comparable to human cortical bone.

In addition to having sufficiently high strength, the effective elastic constants (EECs) of the scaffold must be similar to those of the surrounding tissue in order to guarantee proper load transfer and avoid stress shielding and hence bone resorption [3, 4]. Solution for the EECs (using homogenization) is typically embedded within the topology optimization

methods [11, 12], which are very useful as they provide computational framework for studying effects such as bone remodelling [13] and also allow for efficient design and manufacturing of scaffolds balanced for a specific purpose. Nevertheless, these methods were mostly used to address additive manufacturing technologies other than DIW and it is also not common to detail general solution for EECs of individual architectures. The recent exception is the paper by Roberge et. al [14], who addressed the problem of optimization of porosity and stiffness of DIW scaffolds for flat bones by using curvilinear design and additionally provided approximate closed-form solution for the EECs of two-dimensional regular grids.

The aim of this study was to create a credible 3D finite element (FE) model of an idealized regular scaffold fabricated by DIW and estimate its EECs. The present model considers common adjustable parameters (the diameter of the rod, the distance between the rods, and the overlapping of printed layers) and, unlike previous modelling efforts, the contact radius at the joints. Because of complex relationships between input variables, the work is focused on calcium phosphates, more specifically on hydroxyapatite (HA) and β-tricalcium phosphate (β–TCP), with the effective Poisson's ratio of 0.28 [15]. Experimental data, both from the literature and data obtained from in-house produced β–TCP scaffolds and solid cylinders, were used to validate the model.

2. Numerical homogenization of a scaffold

The FE simulations were carried out using ANSYS software. The tetrahedral elements with quadratic interpolation functions were used for discretization of all models. The initial FE model comprised of a cubic scaffold and two parallel rigid plates. Applied loading and boundary conditions corresponded to compression and shear loading. The contact between the scaffold and the rigid plates was defined as frictionless for axial loading and as bonded

for shear loading, Fig. 1. The scaffold consisted of orthogonal layers of parallel rods with the diameter of 220 μm, the centre-to-centre distance between the adjacent rods on the same printing plane of 300 μm, and the overlap between the printed layers of 50 μm (~23% of the diameter of the rod). This is the same geometry as that of scaffolds studied both experimentally and numerically by Miranda et. al [16-19]. The rods were considered to be made of an isotropic microporous material with properties corresponding to β–TCP [18, 19]: effective Young´s modulus $E^{\mathrm{eff}}_{\mathrm{BULK}}$ = 36 GPa, Poisson´s ratio $\nu^{\mathrm{eff}}_{\mathrm{BULK}}$ = 0.28, and shear modulus $G^{\mathrm{eff}}_{\mathrm{BULK}} = E^{\mathrm{eff}}_{\mathrm{BULK}}/2(1+\nu^{\mathrm{eff}}_{\mathrm{BULK}})$ = 14 GPa.

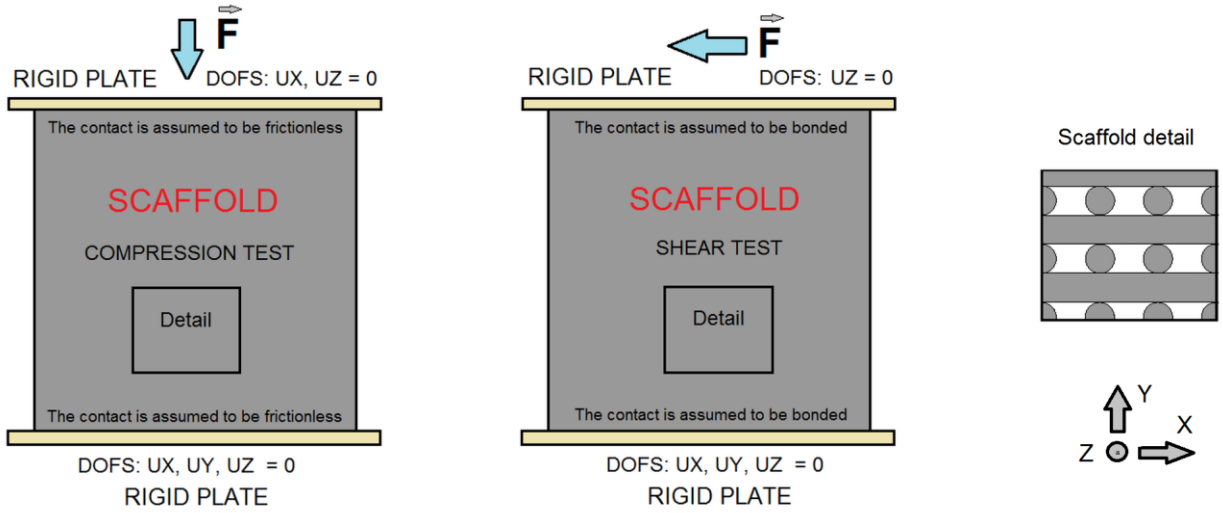

Fig. 1. The loading and boundary conditions applied to FE model of a scaffold cube.

The studied scaffolds belong to the category of orthotropic tetragonal materials that have a pair of coordinate directions along which the elastic constants are identical. The effective elastic tensor $\mathbf{C}^{\mathrm{eff}}$ is thus defined by six independent constants $E,\ E',\ \nu,\ \nu',\ G, G'$:

$$E^{\mathrm{eff}}_{\mathrm{x}} = E^{\mathrm{eff}}_{\mathrm{z}} = E,\ E^{\mathrm{eff}}_{\mathrm{y}} = E',\ \nu^{\mathrm{eff}}_{\mathrm{xz}} = \nu^{\mathrm{eff}}_{\mathrm{zx}} = \nu,\ \nu^{\mathrm{eff}}_{\mathrm{yx}} = \nu^{\mathrm{eff}}_{\mathrm{yz}} = \nu',\ \nu^{\mathrm{eff}}_{\mathrm{xy}} = \nu^{\mathrm{eff}}_{\mathrm{zy}} = \nu'\frac{E}{E'},\ G^{\mathrm{eff}}_{\mathrm{xz}} = G,\ G^{\mathrm{eff}}_{\mathrm{xy}} = G^{\mathrm{eff}}_{\mathrm{zy}} = G'. \quad (1)$$

These constants were obtained by homogenization of the scaffold. The homogenization is a numerical procedure in which the EECs of a continuum are computed from the force-displacement responses of a discrete cellular structure. Using this procedure, it was shown

[20] that $\mathbf{C}^{\mathrm{eff}}$ depends on the number of cells (periodic representative volume elements) per length of the scaffold edge NC as follows:

$$\mathbf{C}^{\mathbf{eff}} = \mathbf{C}_1 + \frac{\mathbf{C}_2}{NC}, \tag{2}$$

where $\mathbf{C}_1$ and $\mathbf{C}_2$ are, respectively, constants related to cells which are not adjacent to the scaffold edges and to cells adjacent to the edges.

The effect of scaffold size on the Young´s moduli and the shear moduli is shown in Fig. 2, where $E_{\mathrm{NC}}^{\mathrm{eff}}$ and $G_{\mathrm{NC}}^{\mathrm{eff}}$ are size-dependent and $E_{\infty}^{\mathrm{eff}}$ and $G_{\infty}^{\mathrm{eff}}$ are size-independent effective constants. It is seen that the size effect is disappearing for $NC \cong 20$. At this point, the errors in Young's moduli E' and E are vanishingly small (less than 0.25 %), E' (modulus in the longitudinal direction, perpendicular to the printing plane, Y- direction in Fig. 1) being underestimated and E (transverse direction, along the rods, X- and Z- directions) being overestimated. The errors in G and G' are larger (~3 %) and, interestingly, both G and G' show the same response. This fact can be explained based on the consideration of deformation of the rods under shear loading. The rods are connected (both in reality and in our model) because of the overlap which causes that they are bent. Due to these interconnections, the force-displacement response under shear is the same in all directions.

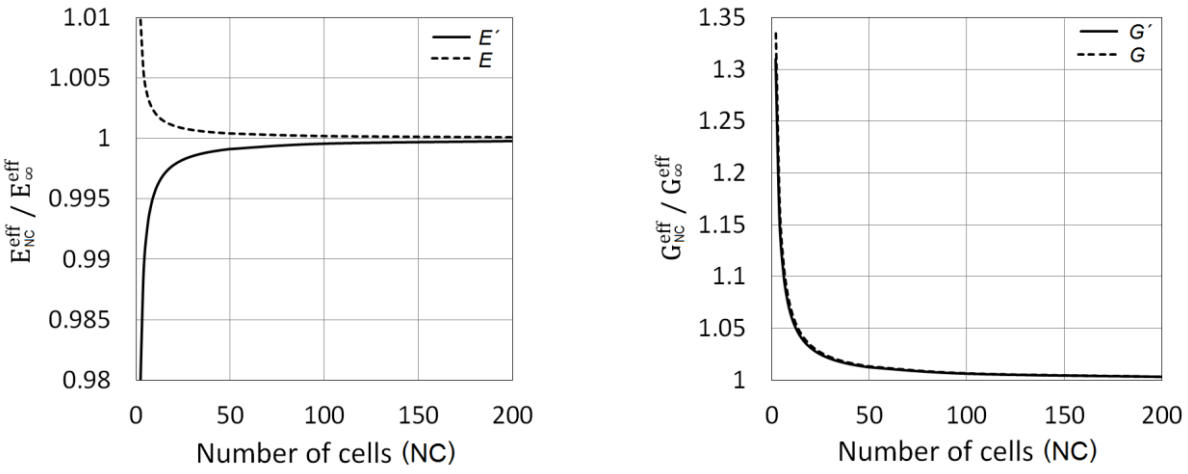

Fig. 2. Normalized Young´s moduli and shear moduli plotted against the scaffold size.

The size of the scaffold of $NC = 20$ is usually easily reachable experimentally because the printed structures are almost not limited by size. Nevertheless, a full FE model of such large scaffold is computationally costly and it practically excludes the possibility to model fine geometrical details (such as the contact radius) having fine discretization at the same time. Due to these limitations, the initial FE model of the scaffold (Fig. 1) was reduced to only one basic cell. By using the periodic conditions and symmetry planes, the final FE model for compression test (Fig. 3) represents the scaffold with infinite dimensions. This allows to take into account the contact radius between the rods and the elastic response is not affected by size.

The *in silico* compression test was used to obtain constants E', ν', E, and ν by applying compressive loading in longitudinal and transverse directions. The parametric study included variations of the diameter of the rod D, the centre-to-centre distance L, the overlap of printed layers P, and the contact radius R. The first three parameters (D, L, P) are directly controlled during computer aided manufacturing, while R is arising from the rheological properties of the ink, as well as printing, drying and sintering conditions.

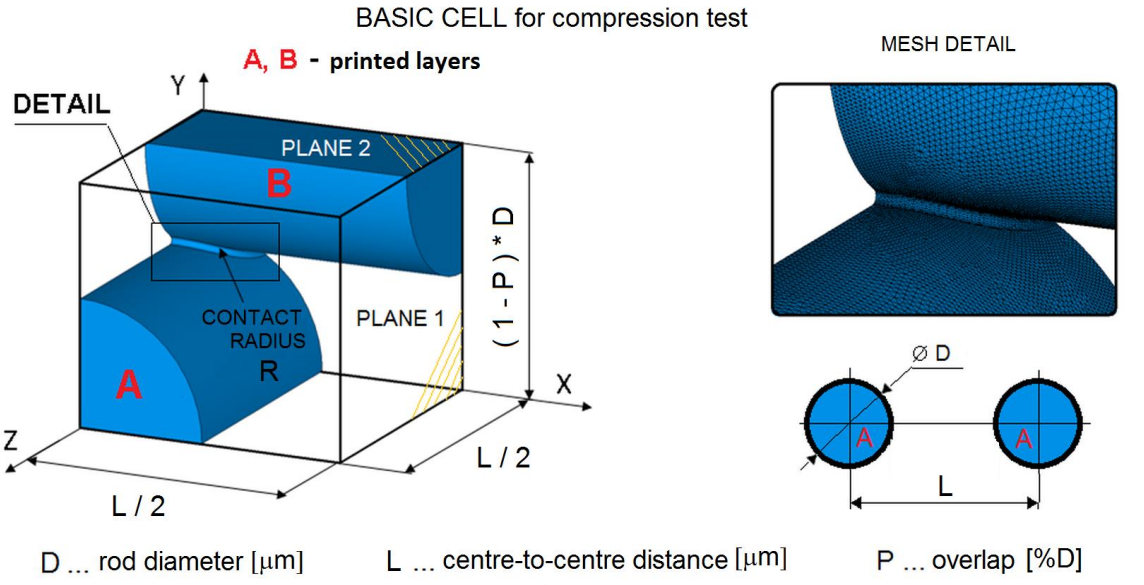

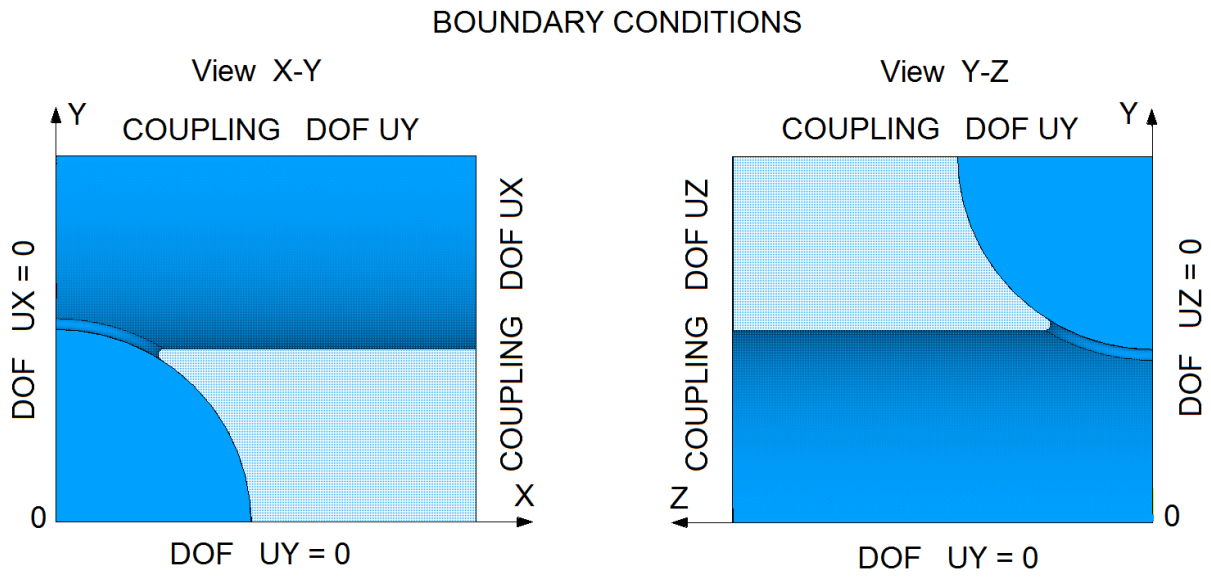

Fig. 3. Finite element model of a basic cell used in the compression test.

The effective shear moduli G' and G, were obtained from the shear test. In this case, the basic cell used for the compression test cannot be employed because it does not allow to prescribe appropriate periodic boundary conditions which define anti-symmetric behaviour. The new basic cell for the shear test was constructed by mirroring the basic cell for the compression test across the plane 1 and then across the plane 2, Fig. 3. The anti-symmetric behaviour for shear test in the X-direction was then realized by prescribing coupling DOFs (degrees of freedom) in Y- and Z- directions, Fig. 4.

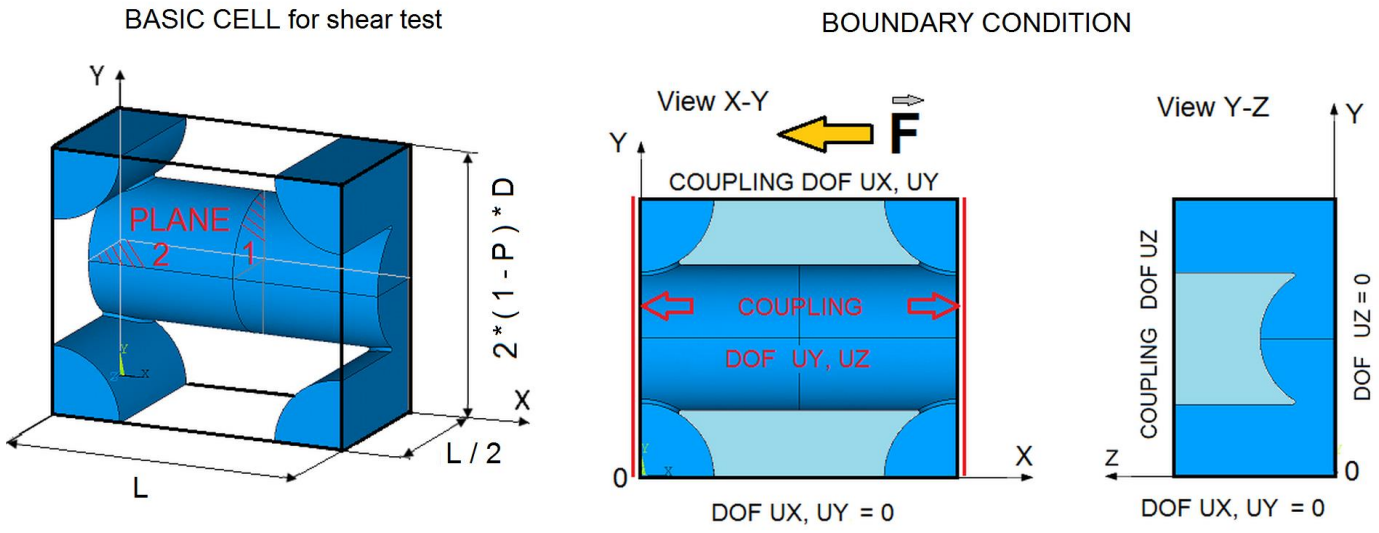

Fig. 4. Finite element model of a basic cell used in the shear test.

The model for the shear test represents the scaffold with infinite dimensions in transverse directions and with finite size in the longitudinal Y-direction. In this case, the boundary layer effect exists near the contact between the scaffold and the rigid plates and it must be taken into consideration. The influence function constants C_1 and C_2 are obtained directly from Eq. (2) for two scaffolds of different sizes. Here, the parameter *NC* denotes the number of basic cells in relevant direction (e.g. Y-direction for shear loading in X-direction, Fig. 4). The constant C_1 is primarily searched because it is related to the value of size-independent shear modulus.

3. Results and discussion

3.1. Effective elastic constants

The EECs were calculated from the two above described tests based on the obtained force-displacement responses. Fig. 5 shows the effective Young´s moduli as a function of the overlap P and the contact radius R (both expressed as percentage of rod diameter D). The plotted values represent the moduli E' and E normalized by the effective modulus of the bulk ($E_{\mathrm{BULK}}^{\mathrm{eff}}$ = 36 GPa) and correspond to the scaffold with the centre-to-centre distance L equal to double of the diameter of the rod ($L = 2D$), refer to Fig. 3.

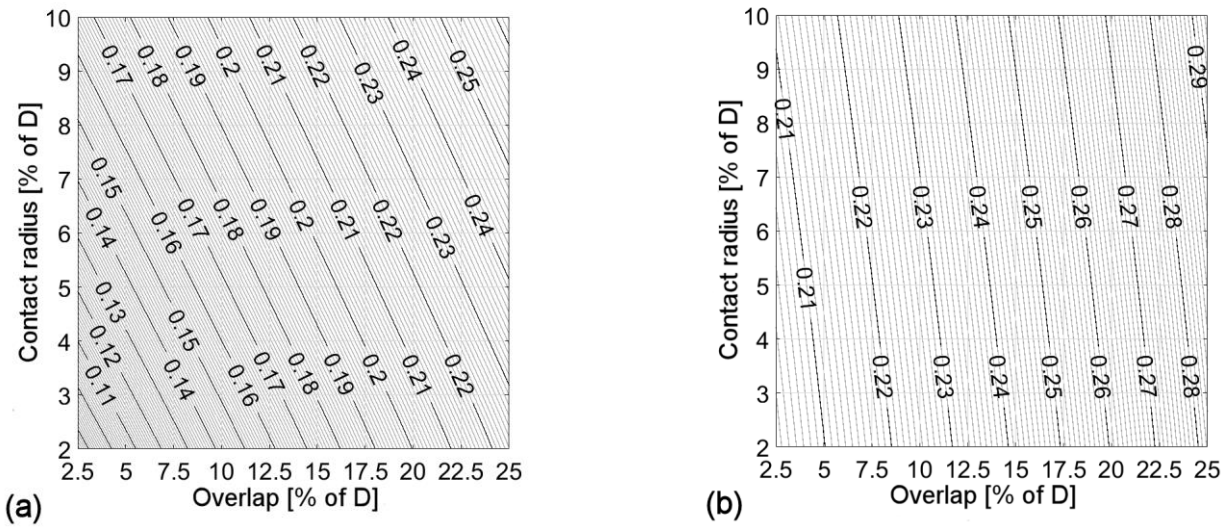

Fig. 5. Normalized Young´s moduli $\frac{E'}{E_{\mathrm{BULK}}^{\mathrm{eff}}}$ in longitudinal (a) and $\frac{E}{E_{\mathrm{BULK}}^{\mathrm{eff}}}$ in transverse (b) directions for $L = 2D$.

As expected, both moduli increase with increasing overlap and increasing contact radius. Within the studied range, the longitudinal modulus E' is somewhat lower ($E' \sim 0.1$ $E_{\mathrm{BULK}}^{\mathrm{eff}}$ for small overlap and small contact radius) than the transverse modulus E ($E \sim 0.2$ $E_{\mathrm{BULK}}^{\mathrm{eff}}$ for small overlap). E' is also quite sensitive to contact radius changes, especially for small overlap. In contrast, E is not very sensitive to the contact radius. Fig. 6 shows the results for the effective Poisson´s ratio, again, for scaffolds with $L = 2D$. In this case, ν is much smaller than ν', corresponding with the limited longitudinal expansion of a scaffold when compressed transversely along the rods. Both parameters are influenced by the contact radius. The scale factors needed to obtain the Young´s moduli and Poisson´s ratios for scaffolds of different geometries ($L \neq 2D$) are plotted in Fig. 7. Note that for scaffolds with $L < 2D$, the scale factor for E' is higher than that for E and that this behaviour reverses for $L > 2D$. In contrast, the scale factors for the Poisson's ratios differs only for low porosities.

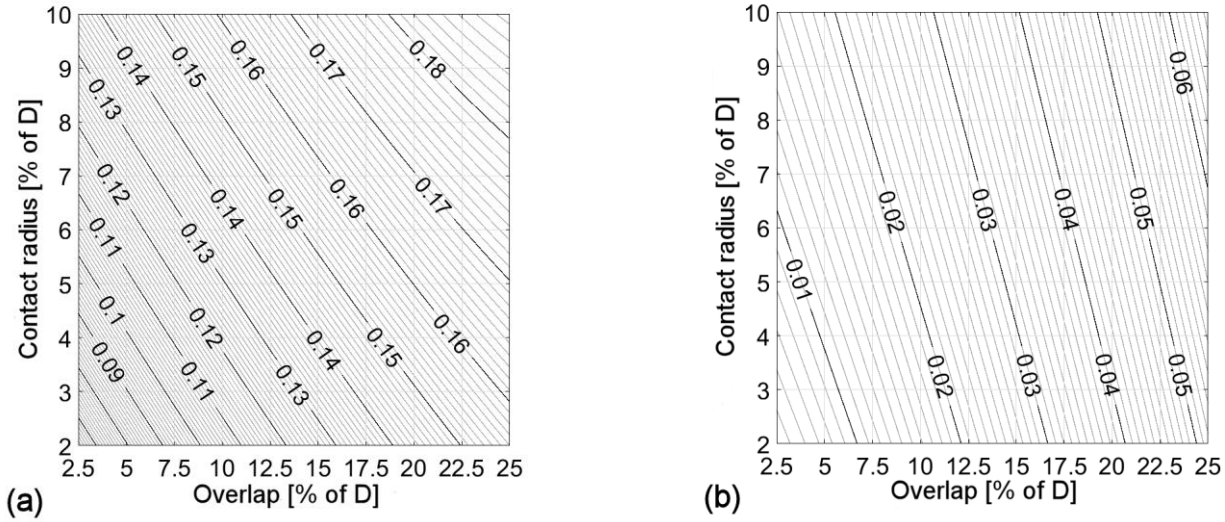

Fig. 6. Poisson´s ratios ν' (a) and ν (b) for $L = 2D$.

The effective shear modulus G normalized by the effective modulus of the bulk ($G_{\mathrm{BULK}}^{\mathrm{eff}}$ = 14 GPa) for the scaffold with $L = 2D$ and the scale factors needed for different geometries

are shown in Fig. 8. Also in this case, the contact radius markedly affects the outputs. Altogether, the results revealed that the effect of contact radius is insignificant only for transversal modulus E, while the other constants are sensitive to this parameter, especially for small overlaps. For instance, if we consider overlap P = 2.5 %, the percentage difference between the values of E', ν, ν', and G for R = 2% and R =10 % is 65 (E') – 115 (ν) %. For overlap P = 20 %, the differences reduce to 20 (E') – 30 (ν, G) %.

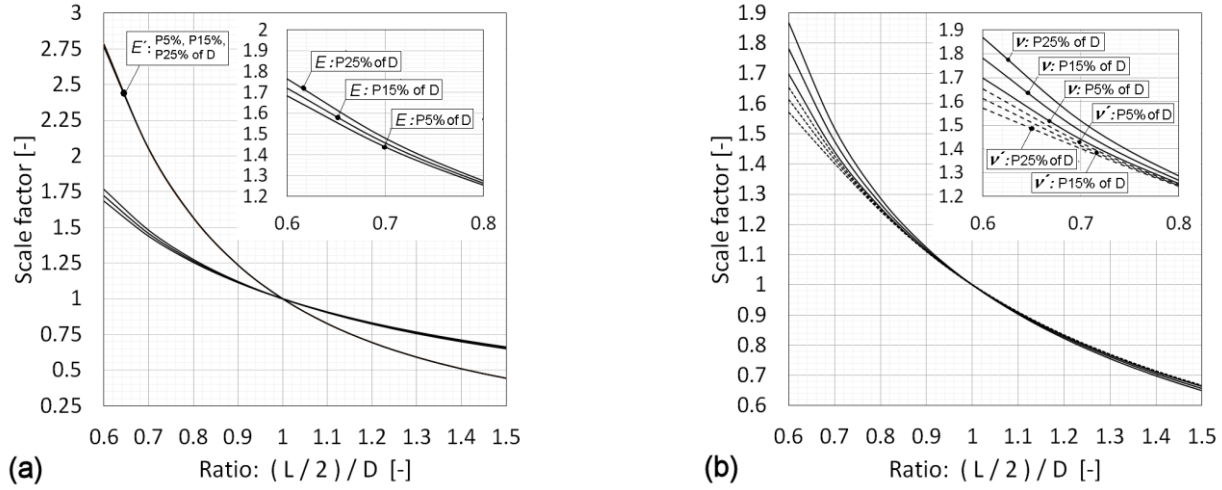

Fig. 7. Scale factors for calculations of Young´s moduli (a) and Poisson´s ratios (b).

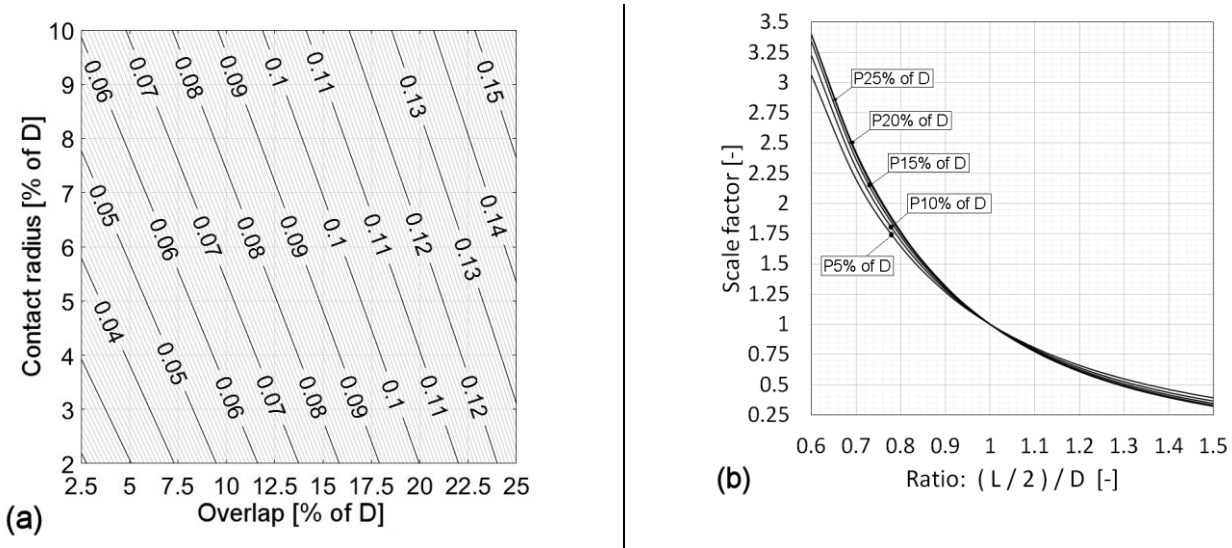

Fig. 8. Normalized shear modulus $\frac{G=G'}{G_{\mathrm{BULK}}^{\mathrm{eff}}}$ for L = 2D (a) and its scale factors (b).

Figs. 5–8 allow determination of the EECs for any combination of input parameters ($E_{\mathrm{BULK}}^{\mathrm{eff}}$, L, D, P, and R). The results are valid for materials with $\nu_{\mathrm{BULK}}^{\mathrm{eff}}$ = 0.28, such as HA or

β-TCP [15]. For materials with different bulk Poisson's ratio, the EECs are different and it is outside the scope of this paper to quantify them. It is sufficient to observe that for scaffolds with P = 20 % and R = 5 % made of bioglass with $\nu_{\mathrm{BULK}}^{\mathrm{eff}}$ = 0.22, the percentage change in predicted E', ν', and G' (with respect to the material group with $\nu_{\mathrm{BULK}}^{\mathrm{eff}}$ = 0.28) are, respectively, -0.4 %, -18.8 %, and -1.2 %, while for scaffolds made of Ti/Al/V alloy with $\nu_{\mathrm{BULK}}^{\mathrm{eff}}$ = 0.34, they are 0.5 %, 19.4 %, and 1.5 %.

3.2. Model validation

The model was tested against the experimental data from uniaxial compression tests of scaffolds made of HA reported by Miranda, et al. [17]. The samples were cubes, approximately 2 × 2 × 2 mm in size, cut out from scaffolds with D = 220 μm, L = 300 μm, and overlap P = 50 μm (same dimensions as those of the β-TCP scaffolds referred to above [18]). The contact radius between the rods was not reported but it can be estimated from provided images that $R \approx$ 15 μm. The effective properties were assumed to be $E_{\mathrm{BULK}}^{\mathrm{eff}}$ = 82 GPa and $\nu_{\mathrm{BULK}}^{\mathrm{eff}}$ = 0.28 [17].

For input P (~22.7 % of D) and R (~6.8 % of D), it is seen from Fig. 5 that the Young's moduli of a scaffold with $L = 2D$ are predicted to be $E' = 0.2393\, E_{\mathrm{BULK}}^{\mathrm{eff}}$ and $E = 0.2781 E_{\mathrm{BULK}}^{\mathrm{eff}}$. The scaffolds studied in [17] have L / $2D$ = 0.6818 and hence by using the scale factors from Fig. 7a one finds that $E' = 0.2393\, E_{\mathrm{BULK}}^{\mathrm{eff}}$*2.1547 and $E = 0.2781 E_{\mathrm{BULK}}^{\mathrm{eff}}$*1.5388, yielding $E' \approx$ 42.3 GPa and E ≈ 35.1 GPa. Using Figs. 6, 7b, and 8 in the same manner, the predicted Poisson´s ratios and the shear modulus are $\nu' \approx$ 0.246, $\nu \approx$ 0.085, and $G = G' \approx$ 11.2 GPa, respectively. In comparison, closed-formed approximate solution for E, ν', and G provided for scaffolds with no contact radius in [14] gives $E \approx$ 40.7 GPa (~15 % difference), $\nu' \approx$ 0.246 (no difference), and $G = G' \approx$ 4.81 GPa (~80 % difference).

Unexpectedly, the experimental data in [17] show that the effective Young's moduli of these scaffolds are in fact much lower than the numerical predictions. The apparent moduli estimated from raw, uncorrected load–displacement data are E' = 3.7–4.2 GPa and E = 2.4–4.4 GPa (first two bars in Fig. 9), and it was later evaluated by Miranda and co-workers that the longitudinal modulus E' = 7 ± 2 GPa, with the compliance of the testing machine taken into account [18]. While it certainly can be agreed that such estimates of Young's modulus from load–displacement responses are inaccurate even with correction for stiffness of the load chain because of possible cracking in the scaffold structure at very low loading during the initial contact with the plates, as argued in [18], the difference of one order of magnitude is not easily explained solely by such effects.

It is to be noted that the tested cubes have finite size (~7 rods in transverse and ~12 rods in longitudinal directions), the effect of which is apparently not significantly important for Young's moduli (Fig. 2). Note also that there is frictional interference between the sample and the plates, the effect of which is more difficult to estimate. As an additional factor, impression in measurements of bulk properties might influenced the outputs of the model as well. In particular, the Young's modulus $E^{\mathrm{eff}}_{\mathrm{BULK}}$ = 82 GPa seems to be rather high for HA with around 15% reported microporosity, although this figure is not entirely unrealistic [21]. In [18], $E^{\mathrm{eff}}_{\mathrm{BULK}}$ was measured by instrumented indentation, with imprint size of about 40 μm and depth of about 5.5 μm that appear to be rather low for microstructure with pores as large as ~10 μm. It is likely that the scale effect was still important and the global property was not measured, similarly to indentation response of heterogeneous alumina and steel coatings studied by Nohava, et al. [22].

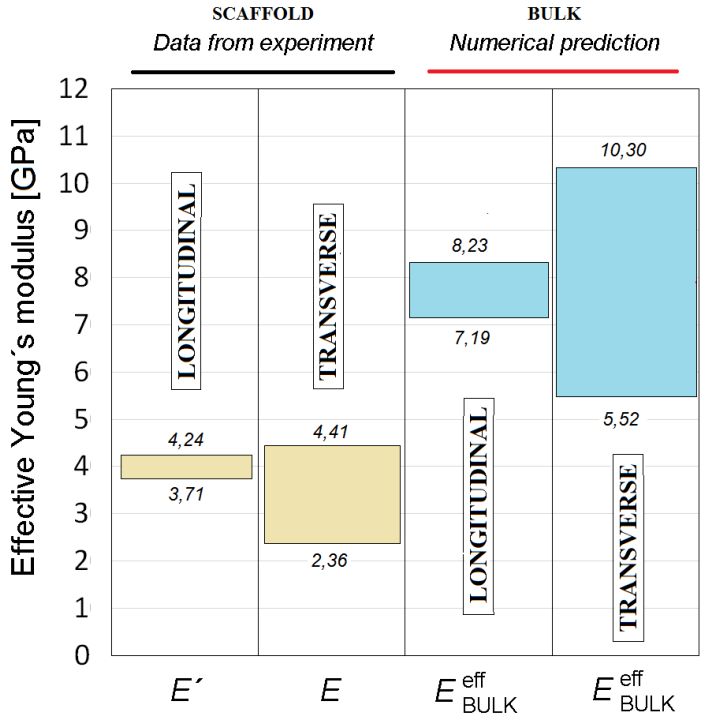

Fig. 9. The effective Young´s modulus of HA scaffolds and inverse estimation of the effective bulk modulus. Values shown in this chart were obtained from load–displacement curves in [17], with no correction for stiffness of the loading chain.

Since E and E' depend on bulk properties, they can be reconverted, which yields $E^{\mathrm{eff}}_{\mathrm{BULK}}$ ~ 7.8 GPa, or $E^{\mathrm{eff}}_{\mathrm{BULK}}$ ~ 13.6 GPa if based on the stiffness-corrected estimate of E'. Although, conversely, these values are rather low in comparison with the assumed value, which means that the precise experimental measurement of scaffold's deformation was indeed required, the estimates of $E^{\mathrm{eff}}_{\mathrm{BULK}}$ obtained from longitudinal and transverse directions are on average almost the same (Fig. 9). This latter result indirectly validates the model developed in this work. Furthermore, it also gives evidence that the scaffolds correctly replicate the desired geometry and were well sintered, as also seen on images in [18].

To further validate the model, we fabricated and tested a set of β-TCP scaffolds and solid cylinders. The ink consisted of the commercial β–TCP powder (VWR Chemicals, USA) and 40 % Pluronic F 127 (Sigma Aldrich, USA) aqueous solution mixed in a 1:1 mass ratio.

Cubic scaffolds (11 mm per side) were printed in air using the robotic deposition device (Pastecaster, Fundació CIM, Spain) equipped with the 610 μm dispensing nozzle (SmoothFlow Tapered Tips, Nordson EFD, USA). Monolithic cylinders, with diameter of 5 mm and height of about 12 mm, were moulded from the same ink. The specimens were dried at room temperature for 24 h and sintered in a muffle furnace in air at 1200 °C for 5 h. Compression tests were performed using a universal testing machine (Instron 8874, USA) at a constant crosshead speed of 0.5 mm/min. The effective Young´s moduli were determined from load–displacement data, which were corrected for stiffness of the load chain. The geometrical parameters determined from scanning electron microscope (TESCAN Lyra3, Czech Republic) images were as follows: D = 538.6 ± 23.3 μm, L = 784.9 ± 32.8 μm, P = 92.1 ± 29.7 μm (17.1 ± 5.5 % of D), and R = 23.1 ± 5.6 μm (4.3 ± 1.0 % of D).

The aggregated results are presented in Fig. 10, where the first bar represents the effective Young's modulus of the bulk obtained from tests on cylinders, the next two columns display the model's outputs for longitudinal and transverse directions, and the last two columns show the corresponding experimental results from the scaffolds. The values of $E_{\mathrm{BULK}}^{\mathrm{eff}}$ evaluated for cylinders show some variability, which is most probably due to randomly distributed superficial irregularities after demoulding. The experimental values of transverse modulus E are in a very good agreement with predictions. On the other hand, experimental values of longitudinal modulus are about 2–5 times lower than the predictions.

There are several possible explanations for low values of E', but the exact causes are presently not known. One possible reason is higher sensibility of the longitudinal modulus to R (Fig. 5), which somewhat varies among the joints. Other possible cause is the fact that the agreement with idealized geometry was not perfect. The rods were slightly

curved due to the gravitational force and there was also certain misalignment of the rods in different layers, which causes bending moments in columns and therefore reduces the longitudinal modulus E'. The transversal modulus is unaffected by such misalignment since in this case the load is transferred along the rods. The average value of the effective Young's modulus of the bulk estimated from all scaffolds' data using an inverse procedure is $E_{\mathrm{BULK}}^{\mathrm{eff}}$ = 0.43 GPa, which is still within the range of the experimental data. Thus despite that the experimental endeavour pointed to some difficulties in preparing ideal designed structures, the results confirm the validity of the model.

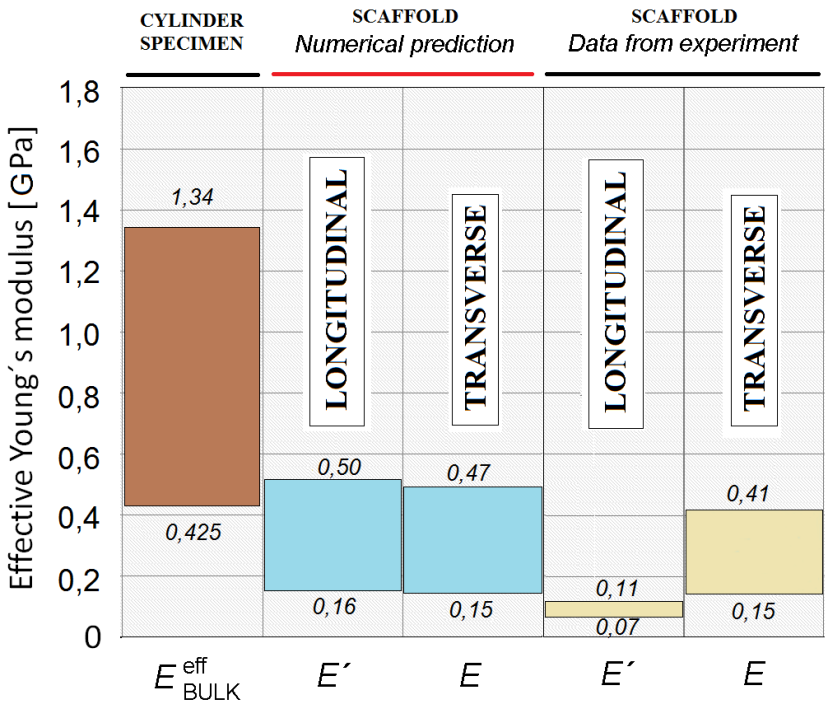

Fig. 10. The effective Young´s modulus of β-TCP solid cylinders and scaffolds.

4. Conclusions

In summary, we derived the general solution of the theoretical effective elastic constants of calcium phosphate scaffolds. The scaffolds were modelled as regular layers of interpenetrating cylindrical rods with the contact radius at the joints, which is the geometry frequently seen in experimental papers. The effect of contact radius was found to be

insignificant only for transversal modulus E and it was important for all other elastic constants, especially when the overlap between successively printed layers was small. It is evident that the geometry of the joints need to be studied more closely, since it provides means to tune scaffold's stiffness (and strength) with almost no penalty for porosity. Size effect vanishes at $NC \cong 20$ which dictates size required in experiments designed with the intention to determine size-independent elastic response. Finally, the inverse numerical procedure can be used to estimate bulk properties of printed material based on data obtained from scaffolds and may be also used to assess quality aspects of the fabrication process.

Acknowledgments

This project received funding from the European Union's Horizon 2020 research and innovation programme under the Marie Skłodowska-Curie and it is co-financed by the South Moravian Region under grant agreement no. 665860. Authors also acknowledge the project CEITEC 2020 (LQ1601) with financial support from the Ministry of Education, Youth and Sports of the Czech Republic under the National Sustainability Program II. Special thanks to Eng. Mariano Casas-Luna and Eng. Carmen Hernandez-Escalera, for their support during DIW and sintering of the scaffolds.

References

[1] M.M. Stevens, Biomaterials for bone tissue engineering, *Mater. Today* **11** (2008) 18-25.

[2] A.J.W. Johnson, B.A. Herschler, A review of the mechanical behavior of CaP and CaP/polymer composites for applications in bone replacement and repair, *Acta Biomater.* **7** (2011) 16-30.

[3] S. Bose, M. Roy, A. Bandyopadhyay, Recent advances in bone tissue engineering scaffolds, *Trends Biotechnol.* 30 (2012) 546-554.

[4] M.A. Velasco, C.A. Narváez-Tovar, D.A. Garzón-Alvarado, Design, materials, and mechanobiology of biodegradable scaffolds for bone tissue engineering, *Biomed Res. Int.* 2015 (2015) 21.

[5] J.A. Lewis, Direct ink writing of 3D functional materials, *Adv. Funct. Mater.* 16 (2006) 2193-2204.

[6] Q. Fu, E. Saiz, A. Tomsia, Bioinspired strong and highly porous glass scaffolds. *Adv. Funct. Mater.* 21 (2011) 1058-1063.

[7] A. Bignon, J. Chouteau, J. Chevalier, G. Fantozzi, J.P. Carret, P. Chavassieux, G. Boivin, M. Melin, D. Hartmann, Effect of micro- and macroporosity of bone substitutes on their mechanical properties and cellular response, *J. Mater. Sci. Mater. Med.* 14 (2003) 1089-1097.

[8] V. Karageorgiou, D. Kaplan, D. Porosity of 3D biomaterial scaffolds and osteogenesis. *Biomaterials* 26 (2005) 5474-5491.

[9] H. Shao, Y. He, J. Fu, D. He, X. Yang, J. Xie, C. Yao, J. Ye, S. Xue, Z. Gou, 3D printing magnesium-doped wollastonite/β-TCP bioceramics scaffolds with high strength and adjustable degradation, *J. Eur. Ceram. Soc.* 36 (2016) 1495-1503.

[10] S. Eqtesadi, A. Motealleh, P. Miranda, A. Pajares, A. Lemos, J. Ferreira, Robocasting of 45S5 bioactive glass scaffolds for bone tissue engineering, *J. Eur. Ceram. Soc.* 34 (2014) 107-118.

[11] C. Lin, N. Kikuchi, S. Hollister, S., A novel method for biomaterial scaffold internal architecture design to match bone elastic properties with desired porosity, *J. Biomech.* **37** (2004) 623-636.

[12] P. Coelho, S. Hollister, C. Flanagan, P. Fernandes, Bioresorbable scaffolds for bone tissue engineering: Optimal design, fabrication, mechanical testing and scale-size effects analysis, *Med. Eng. Phys.* **37** (15) 284-296.

[13] S. Sturm, S. Zhou, Y. Mai, Q. Li, On stiffness of scaffolds for bone tissue engineering – a numerical study, *J. Biomech.* **43** (2010) 1738-1744.

[14] J. Roberge, J. Norato, Computational design of curvilinear bone scaffolds fabricated via direct ink writing, *Comput. Aided Des.* **95** (2018) 1-13.

[15] C.B. Carter, M.G. Norton, *Ceramics in Biology and Medicine*, In: *Ceramic Materials: Science and Engineering*, 2nd edition, Springer Science+Business Media, New York 2013, DOI 10.1007/978-1-4614-3523-5_35.

[16] P. Miranda, E. Saiz, K. Gryn, A. Tomsia, Sintering and robocasting of β-tricalcium phosphate scaffolds for orthopaedic applications, *Acta Biomater.* **2** (2006) 457-466.

[17] P. Miranda, A. Pajares, E. Saiz, A. Tomsia, F. Guiberteau, Fracture modes under uniaxial compression in hydroxyapatite scaffolds fabricated by robocasting, *J. Biomed. Mater. Res. A* **83A** (2007) 646-655.

[18] P. Miranda, A. Pajares, E. Saiz, A. Tomsia, F. Guiberteau, Mechanical properties of calcium phosphate scaffolds fabricated by robocasting, *J. Biomed. Mater. Res. A* **85A** (2008) 218-227.

[19] P. Miranda, A. Pajares, F. Guiberteau, Finite element modeling as a tool for predicting the fracture behavior of robocast scaffolds, *Acta Biomater.* **4** (2008) 1715-1724.

[20] P. Skalka, P. Navrátil, M. Kotoul, Novel approach to FE solution of crack problems in the Laplacian-based gradient elasticity, *Mech. Mater.* **95** (2016) 28-45.

[21] D.S. Metsger, M.R. Rieger, D.W. Foreman, Mechanical properties of sintered hydroxyapatite and tricalcium phosphate ceramic, *J. Mater. Sci. Mater. Med.* **10** (1999) 9-17.

[22] J. Nohava, R. Mušálek, J. Matějíček, M. Vilémová, A contribution to understanding the results of instrumented indentation on thermal spray coatings — Case study on Al_2O_3 and stainless steel, *Surf. Coat. Tech.* **240** (2014) 243-249.